Electromagnetic Precursors of Earthquakes Mediated by Ground Surface Plasma Wave, Part II: Verification by Numerical Analysis

Masafumi Fujii[*]

October 13, 2022

Abstract

The mechanism of electromagnetic precursors of earthquakes has long been unclear. Owing to the lack of understanding of the electromagnetic behavior of seismic activity, anomalous signals associated with earthquakes have not been recognized as precursors. We show, in this paper by a numerical electromagnetic wave analysis, that when electric charge carriers appear on the ground surface as a consequence of the tectonic stress exerted on the earth's crust, they interact strongly with radio broadcast waves on the ground surface, and eventually radiate precursory signals of earthquakes. The analysis was performed using the three-dimensional finite-difference time-domain (3D-FDTD) method on a massively parallel supercomputer. The numerical models comprise digital elevation models of actual geographic landforms including a peak of mountains or coastlines with high cliffs. The results show the possible mechanisms of electromagnetic precursors, which explain the anomalous electromagnetic signals observed by the authors before earthquakes.

Keypoints

- 3D electromagnetic analyses have been performed for the landforms where anomalous signals were observed before large earthquakes.

- Interaction between radio waves and electrical charge carriers on the ground surface has been modeled by the FDTD method with the Drude dispersion function.

- The electromagnetic precursors of earthquakes are radiated by the ground surface plasma wave manifesting from the electrical charge carriers.

---

[*]Univ. of Toyama, 3190 Gofuku Toyama, Japan

1   Introduction

In Part I [4] accompanying this paper, many examples of the precursors of earthquakes that we detected are reported. In this paper Part II, we analyze the possible mechanism of the precursors caused by an interaction between the ground surface plasma wave and the radio wave near the ground surface. Several analyses have been performed with various landforms of irregular shapes in mountainous regions and coastlines to show that the electromagnetic interactions occur randomly and strongly depending on the topography of the ground surface.

The analysis was performed using the three-dimensional finite-difference time-domain (3D-FDTD) method with the properties of the mobile electric charge carriers of the Drude dispersion model [1, 3]. The analysis method and computational code have been verified by comparing with the theoretical solutions of localized surface plasmons on a metal sphere [2]. This study deals with the actual geographic model of the region where possible earthquake precursors have been detected by the authors as shown in Part I [4]. The polarization of the radio wave was chosen identically to the actual broadcast radio wave, i.e., horizontal polarization. The scattering and diffraction of the radio waves were then analyzed by modeling the behavior of the electric charge carriers on the ground surface. This could be the mechanism of the precursory radio wave signals detected in our observations before earthquakes.

In addition, the behavior of the electric charge carriers varies depending on the shape and physical state of the ground surface. In mountainous regions, the charge carriers repel each other and move to the edges or peaks of mountains, stay there for a certain period until they recombine with opposite charges and disappear. In planar regions, the charge carriers diffuse and spread without remaining in a place, fluctuate, and disappear relatively more quickly than in mountains. Near coastlines with cliffs relatively higher above sea level than the wavelength of the radio wave, rough vertical surfaces may play a role; it is presumed that the radio waves are scattered and diffracted to yield horizontally polarized waves. Because no obstacles are found against the radio waves to propagate on the surface of the ocean, they will reach the distance of the line of sight. The FDTD method is a powerful tool for the analysis of the interaction between surface plasma waves and radio waves. We attempt to elucidate the mechanism of the electromagnetic precursors of earthquakes on real landforms with the method.

2   FDTD Analysis of Electromagnetic Precursors of Earthquakes

We begin with the modeling of the electromagnetic precursors by the 3D-FDTD method with the frequency-dependent Drude dispersion function [1, 2, 3]. The computation was performed on a massively-parallel supercomputer Cray CS400 at Kyoto University, Japan. We used 64 nodes of 2304 central processing unit (CPU) cores with the Message Passing Interface (MPI) libraries and a maximum of 7.8 TB of memory for solving large-scale problems. The digital elevation model (DEM) of the landform has been publicized by the Geographical Survey Institute (GSI), Japan. The resolution of the original DEM used in this study was approximately 5 m within the horizontal surface. The accuracy of the altitude is 0.3 m in standard deviation, which is the most precise model available from GSI at the time of this study.

2.1   Modeling of the surface plasma wave by the Drude dispersion function

The interaction between the ground surface plasma wave and radio wave is effectively modeled by the 3D-FDTD analysis with the Drude dispersion function for the oscillation of charged particles [1, 3]. We define the dielectric properties of the ground that is loaded with the mobile electric charge carriers as in [3]. Damping effects are introduced into the Drude function for considering the lossy objects on the ground such as trees, plants, and wet soils.

It has been estimated that the plasma frequency for the electric charge on the ground surface [3] is given by

$$f_p = \frac{1}{2\pi}\sqrt{\frac{n\,q^2}{\epsilon_0\,m^*}}\;, \tag{1}$$

where the electrical charge q of the particle is that of an electron i.e., $q = 1.60 \times 10^{-19}$ C of either positive or negative charge, $\epsilon_0 = 8.85 \times 10^{-12}$ F/m is the permittivity of vacuum. The number density of charged particles n is determined to be approximately 10^{15} to 10^{16} m^{-3}, which agrees in its order with the experimental evaluation [7] and theoretical considerations [5]. The effective mass of the particle m^* still contains uncertainty in the values to choose, but it is conceivable that it has a value several times larger than the static mass of an electron m_e, i.e., $m^* \approx m_e$ to $10\,m_e$ [3]. In a frequency range lower than f_p, the electric charge carriers oscillate with the outer electric field of the radio wave. Thus, the collective oscillation of the charged particles is induced on the ground surface, i.e., as a surface plasma wave or surface plasmon on the earth.

We consider the boundary between air and ground, i.e., the permittivity of air $\epsilon_1 = \epsilon_0\epsilon_{r1}$ with $\epsilon_{r1} = 1$ and the complex permittivity of the ground $\epsilon_2 = \epsilon_0\epsilon_{r2}$ with

$$\epsilon_{r2} = \epsilon'_{r2} - j\epsilon''_{r2} = \epsilon_\infty - j\frac{\sigma}{\epsilon_0\omega} - \frac{\omega_p^2}{\omega^2 - j\omega\Gamma}\;, \tag{2}$$

where ϵ'_{r2} and ϵ''_{r2} denote the real and the imaginary parts of the complex permittivity ϵ_{r2}, respectively, j the imaginary unit, ϵ_∞ is the relative permittivity of the ground at the limit of infinite frequency, σ is the conductivity of the ground, Γ is the damping factor of the Drude dispersion, and ω is the angular frequency of the radio wave. The second term on the right-hand side represents the loss. The third term is the Drude dispersion, which represents the plasma oscillation of the charged particles in response to the outer electric field [6]. When the permittivity of the ground is larger than that of air, the effective plasma frequency for the plasma oscillation on the ground is obtained by letting eq. (2) $\epsilon_{r2} = 0$, and if $\sigma \ll 1$ and $\Gamma \ll \omega_p$, to give

$$f'_p = \frac{f_p}{\sqrt{\epsilon_\infty}}\;. \tag{3}$$

We consider larger loss factors of Γ in (2) as $\Gamma = 2\pi \times 10^6$ to $2\pi \times 10^8$ rad/s, and assume that $\epsilon_\infty = 6$ for the ground, and that the effective plasma frequency $f'_p = 1000/\sqrt{6} \approx 408$ MHz for all the analysis in this paper. The relative permittivity of the ground in Fig. 1 shows that, with the Γ used in this study, the necessary conditions for the surface plasma waves to be induced, i.e., $\epsilon'_{r2} < 0$ and $|\epsilon'_{r2}| > \epsilon_{r1} = 1$ are still satisfied. As shown in Fig. 2, the effective plasma frequency is sufficiently higher than the radio broadcast frequency of 70 MHz, which is adopted for all the incident waves in this study.
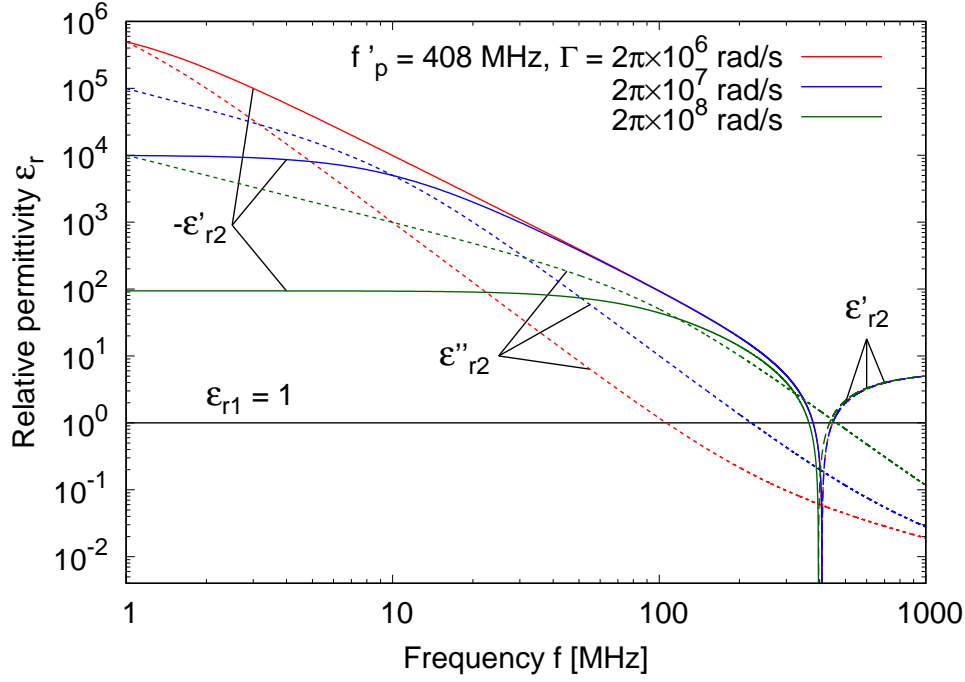
3

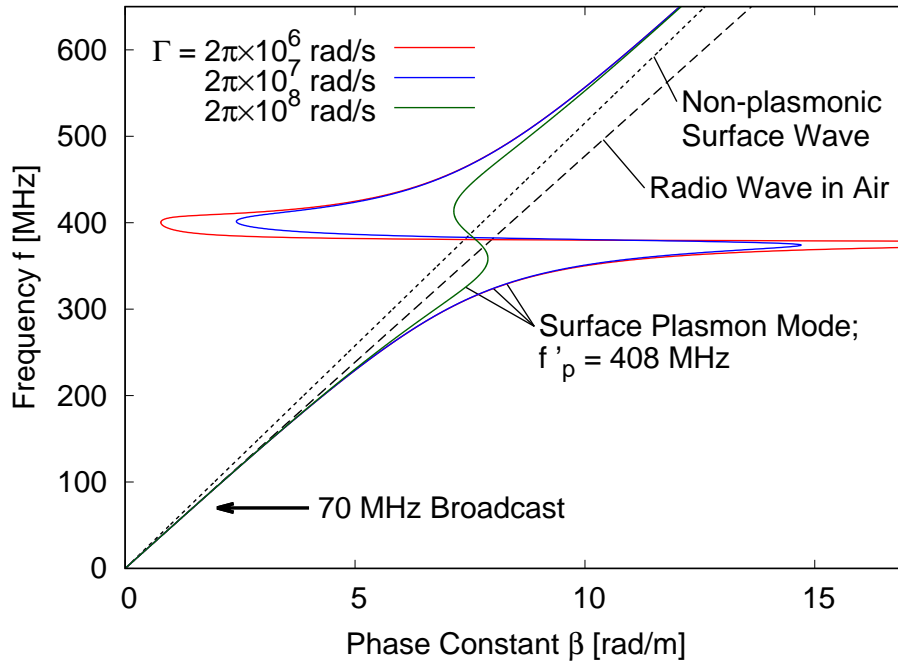Figure 1: Dielectric permittivity model of the ground under electrical charge carriers.

Figure 2: Dispersion diagram of the ground surface plasma wave with a parameter of the damping factor Γ of Drude dispersion.

Table 1: List of the earthquakes discussed in this section. Magnitude M is of JMA. The maximum seismic intensity of Japan scale (Max SI) is also shown.

No.	Epicenter	M	Date	Time (JST)	depth	Max SI
1	Nagano middle part	5.5	April 23, 2020	13:44:22.1	3 km	4
2	Nagano middle part	5.0	April 23, 2020	13:57:55.1	5 km	3
3	Nagano middle part	5.0	April 26, 2020	02:22:49.4	6 km	3
4	Gifu Hida District	5.4	May 19, 2020	13:12:58.1	7 km	4
5	Nagano middle part	5.3	May 29, 2020	19:05:14.9	4 km	4

3 Precursors over Mountainous Region around Kamikochi and Oku-Hodakadake Peak in the Middle Part of Japan

We consider the peak of a mountain located on the way between a broadcast station and an observation station. Many precursory-like signals were observed from 2019 to 2020 around this path of the radio wave, and some period after that, a group of earthquakes occurred in the same district. In mountainous regions, charge carriers may repel each other and move to the sharp edges or peaks of mountains. The charge carriers accumulate and stay on the surface until they recombine with charges of opposite signs and disappear. Radio waves that propagate over the peak of a mountain interact with the charge carriers and cause strong diffraction that would not occur without the charge carriers. The charge carriers then oscillate with the outer electric field of the radio waves, turning to the ground surface plasma wave. Such anomalous electromagnetic diffraction may be detected during radio wave observations as earthquake precursors.

3.1 Observed Electromagnetic Precursors

Radio wave observation was performed with the location of the broadcast and observation stations as shown in Fig. 3. The Iida broadcast station (●, E137° 52'21", N35° 27'33", altitude 770m) is located at a relatively high altitude in Iida City and is surrounded by much higher mountains near 3000 m. Thus, with the usual non-plasmonic diffraction by higher mountains, the radio wave may reach the peak of Oku-Hodakadake (▲, E137° 38'53", N36° 17'20", alt. 3189.5m). The polarization of the broadcast wave was horizontal. The Toyama observation station (■, E137° 11'13", N36° 41'38", alt. 30m) is in Toyama City and is located on top of a building.

In the region of Fig. 3, a group of earthquakes occurred during a short period of April and May, 2020, as shown in Table 1, and the epicenters are shown by red-filled circles in Fig. 3. The region is known for steep mountains, where a group of large earthquakes often occur. Numerous rectangular-shaped radio wave anomalies were observed first as shown in Figs. 4 and 5. The observed anomalies were remarkably clear; interestingly, the width and the height of the anomalies vary from each other. After a few months of a quiet period of no anomalies, a series of earthquakes of over $M5$ occurred as shown in Table 1. After these earthquakes, the rectangular-shaped anomalies have never appeared, except for small ones. These anomalies may have been generated by the interaction between the radio wave and the ground surface plasma wave at the peak of the mountain in this region. The observation method is described in detail in the accompanying paper Part I [4]. Other research groups observed some precursory signals at similar locations with low-frequency geopotential measurements before the 1999 $M4.7$ earthquake [8].
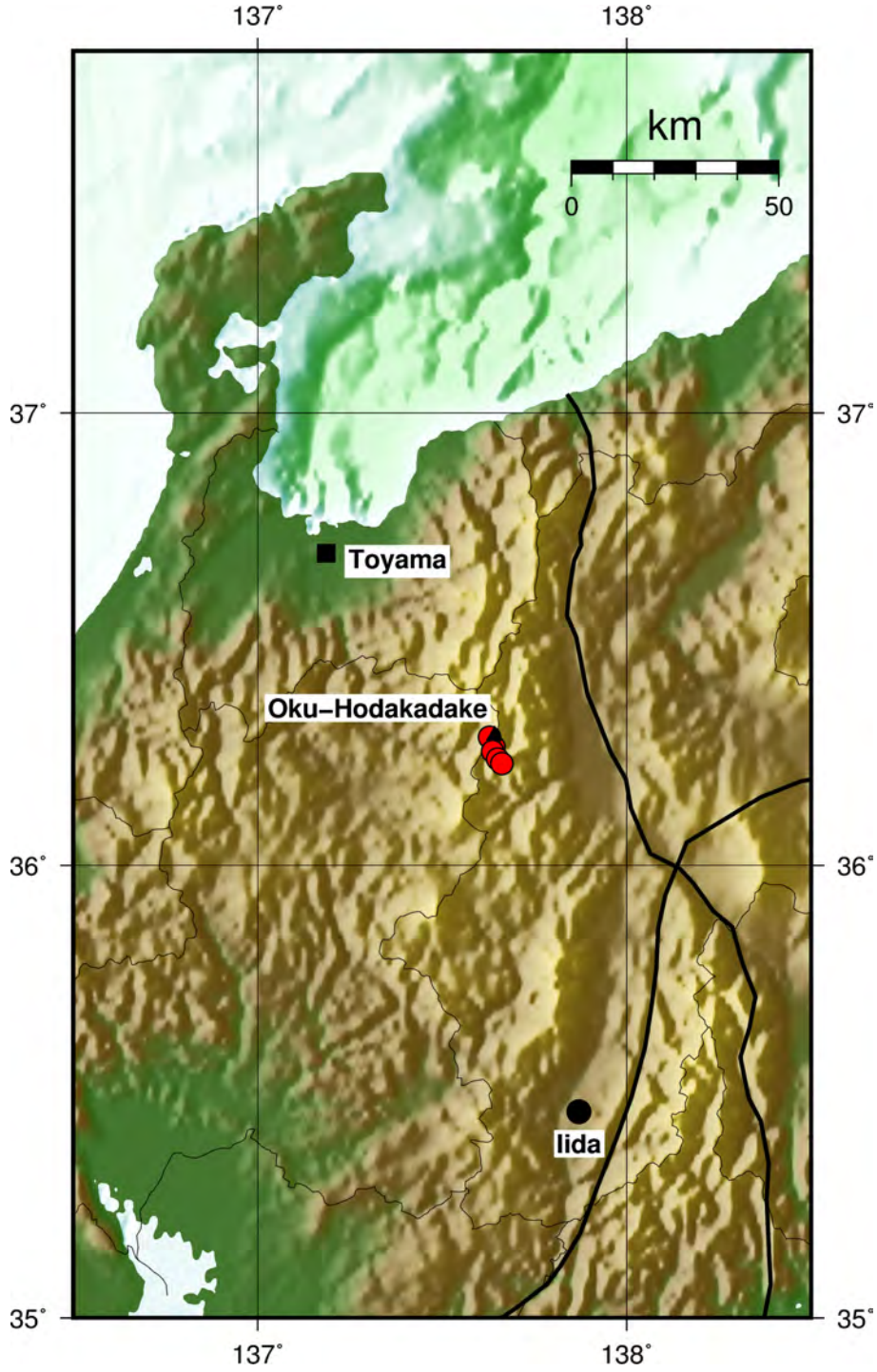
Figure 3: Map of the middle part of Japan near the Oku-Hodakadake peak (▲). The broadcast station (●) in Iida City, the observation station (■) in Toyama City are shown. The epicenters of the earthquakes of Table 1 are shown by red-filled circles at the same location with the Oku-Hodakadake peak. Thick solid lines are a part of the Median Tectonic Line (running from low center to right center) and a part of the Shizuoka-Itoigawa Tectonic Line (running from the seaside to right low). The map was generated with the Generic Mapping Tools (GMT) and the dataset of ETOPO1 Global Relief Model from the NOAA National Centers for Environmental Information, USA. Note the detail of the water surface in the map is partly inaccurate in the ETOPO1 dataset.

(a) 10 days from Dec. 27, 2016

(b) 10 days from May 6, 2019

(c) 10 days from Dec. 2, 2019

(d) 10 days from Dec. 12, 2019

(e) 10 days from Dec. 31, 2019
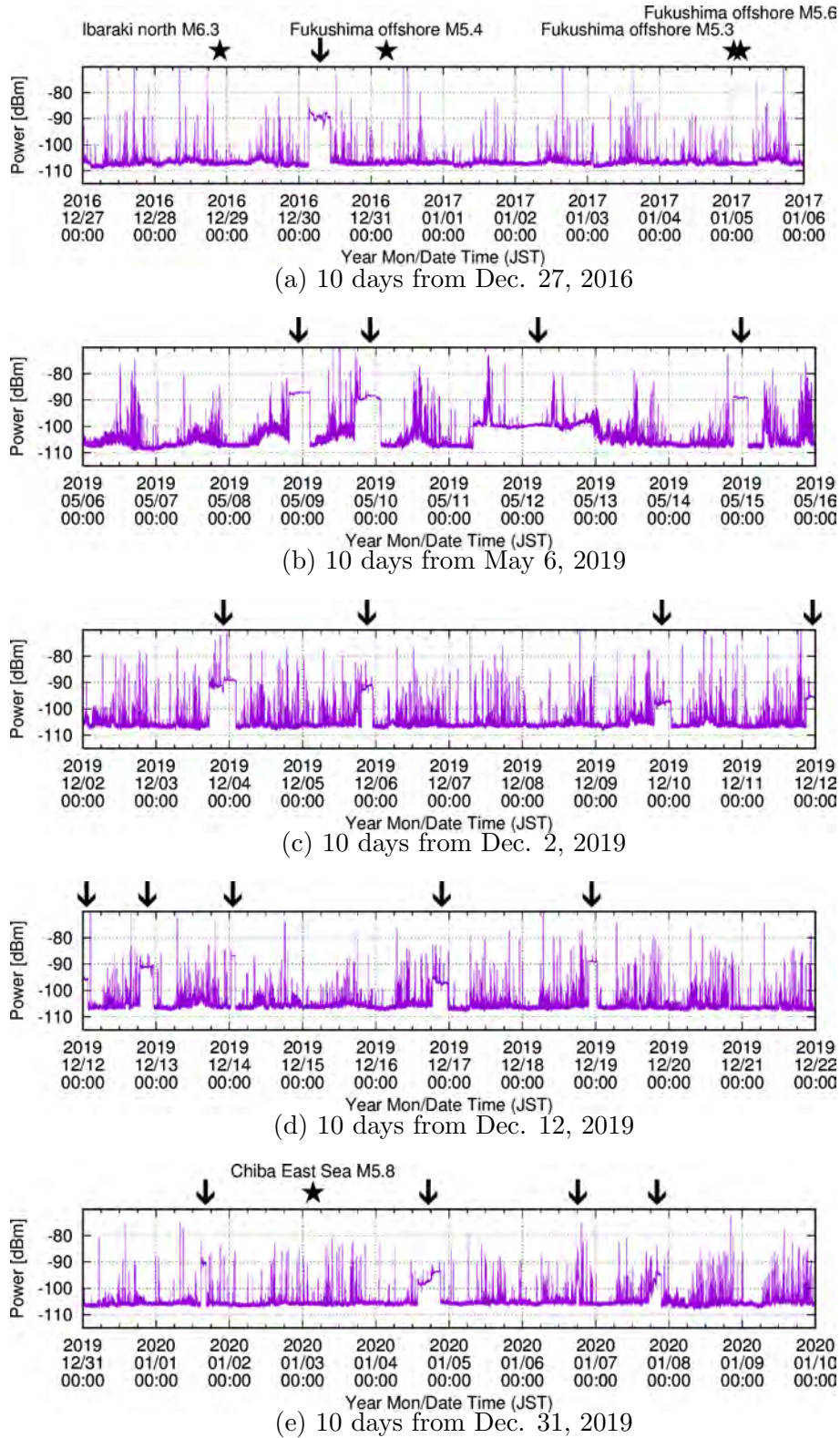
Figure 4: Anomalous electromagnetic wave propagation from Iida to Toyama at 88.3MHz since 2016 till 2020 obtained by the authors. Arrows show the anomalous signals of the radio wave appearing like a random rectangular-shaped pulse. Star notations show the major earthquakes larger than approximately 5 in magnitude (JMA) in the periods. A group of earthquakes occurred in April and May 2020, which is a period after (e). After those earthquakes, precursors are seldom seen. Continue to Fig. 5.

7
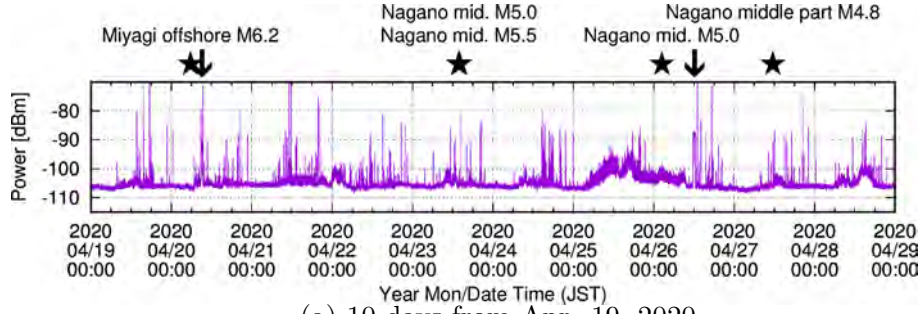
(a) 10 days from Apr. 19, 2020
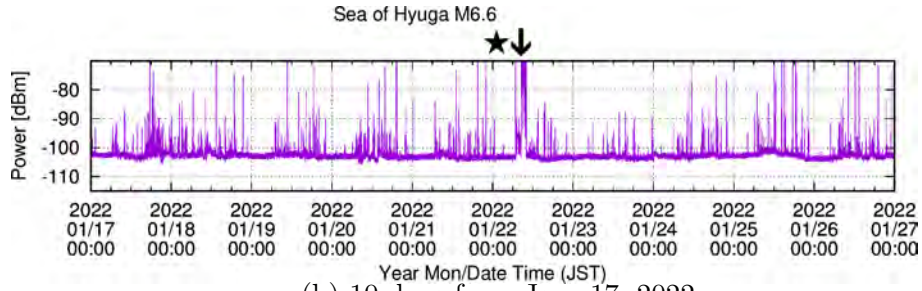
(b) 10 days from Jan. 17, 2022
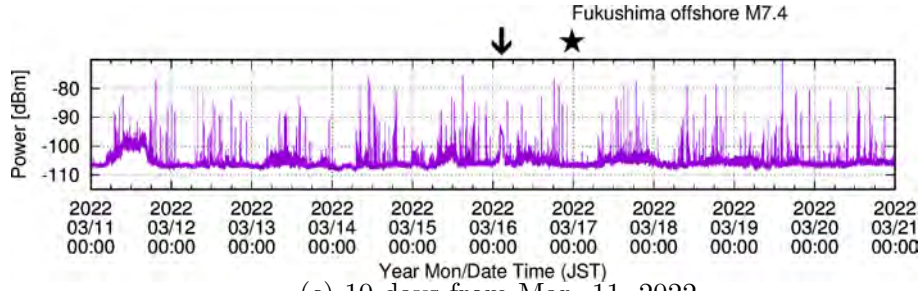
(c) 10 days from Mar. 11, 2022

Figure 5: Continued from Fig. 4. Anomalous electromagnetic wave propagation from Iida to Toyama at 88.3MHz since 2020 till 2022 obtained by the authors. Arrows show the anomalous signals of the radio wave appearing like a random rectangular-shaped pulse. Star notations show the major earthquakes larger than approximately 5 in magnitude (JMA) in the periods. A group of earthquakes occurred in April and May 2020, only large events of which are shown in (a) by starts, and after that period, as in (b) and (c), precursors are seldom seen.
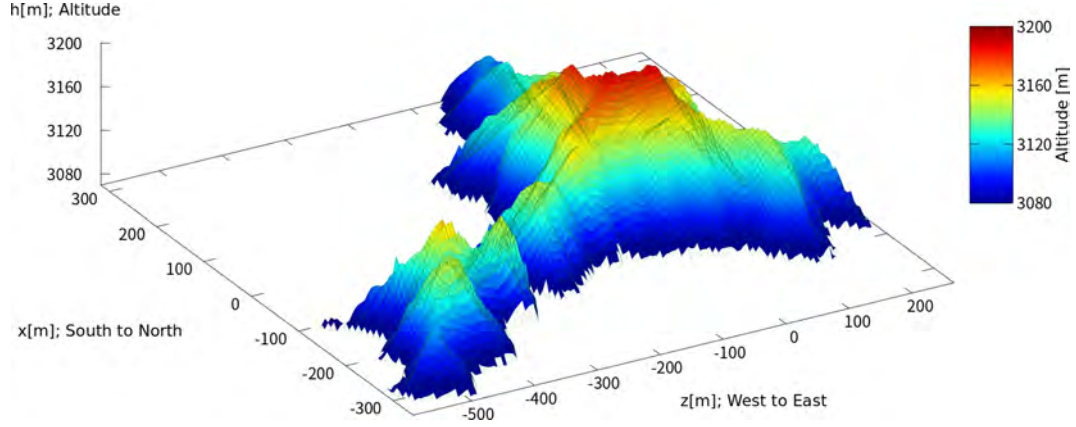
Figure 6: 3D analysis configuration of the Oku-Hodakadake peak of 3189.5 m altitude. Green grid lines show the original digital elevation model of approximately 5m resolution. The origin of the horizontal axes is collocated with the peak. Altitude h is taken in the y-direction. The digital elevation model (DEM) is publicized by the Geographical Survey Institute, Japan.

3.2 Analysis of Anomalous Mountain Diffraction at Oku-Hodakadake Peak in the Middle Part of Japan

We analyzed the interaction between a radio wave and a ground surface plasma wave on the highest peak of Oku-Hodakadake peak in Kamikochi district of the north Japan Alps shown in Fig. 3. The analysis configuration of the peak is shown in Fig. 6. The size of the analysis region is 860 m from west to east, 710 m from south to north including the peak, and an altitude higher than 3070 m was modeled up to 3240 m with a total height of the analysis region of 170 m. The peak is 3189.5 m in altitude, and the space above the peak to the upper boundary is approximately 50 m. The original grid of the DEM in Fig. 6 has approximately 5m resolution, and finer grids of 0.2 m resolution were obtained by spline interpolation for the FDTD analysis. The boundaries of the analysis region were all set to be the perfectly matched layer (PML) absorbing boundary of 50 layers and the reflection of the radio wave from the boundary was minimized. For the whole mountain, the relative dielectric permittivity was set to $\epsilon_\infty = 6$ and the electric conductivity $\sigma = 1.0 \times 10^{-3}$ S/m. The parameters of the Drude dispersion $f'_p = 408$ MHz and two cases of $\Gamma = 2\pi \times 10^7$ and $2\pi \times 10^8$ rad/s were tested for the electrically-charged ground. The required total memory was 5.8 TB with 2304 CPU cores, and the elapsed time was approximately 10 hours for a single run of this analysis.

To model the radio wave propagation in Fig. 3, a radio wave of 70 MHz was incident from the south of the Oku-Hodakadake peak with horizontal polarization E_z. To distinguish the radio wave behavior with and without surface charges, it is better ploting the E_y component in which the incident wave is not included; only the scattered or diffracted wave is observed. The wave then hits the peak. In the case where no earthquake is anticipated and no electrical charge exists, the radio wave is scattered and diffracted as a normal phenomenon at the peak, and the wave partly penetrates the ground. The results are shown in Fig. 7(b). Conversely, in the case where earthquakes are anticipated and electrical surface charges accumulate around the peak, the radio wave is scattered and diffracted strongly into random directions as shown in Figs. 7(c) and (d). This is an anomalous mountain diffraction that is caused only by the peak covered with surface electrical charges.
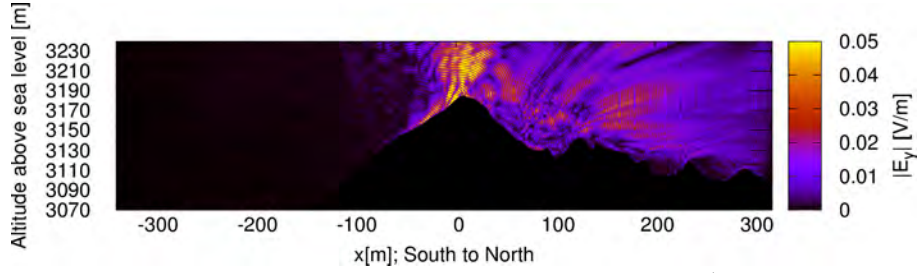
In Figs. 8 and 9, similar effects are clearly observed in the horizontal planes at 3120 m and at 3160 m, respectively. The incident wave was modeled such that it had the highest intensity near
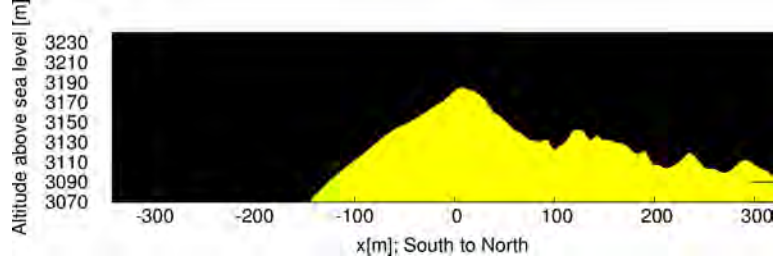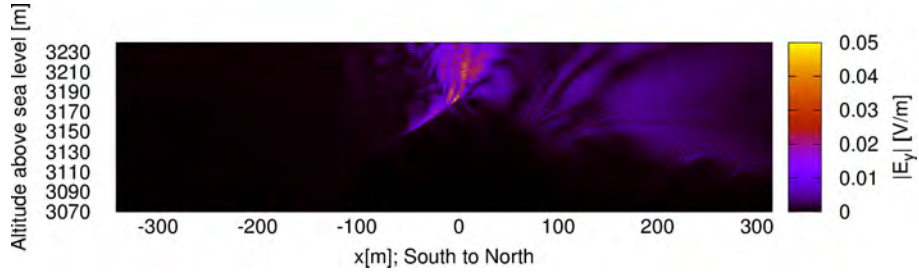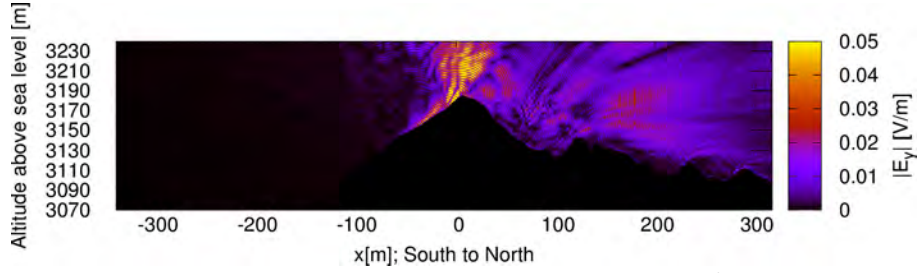
9

(a) Configuration of the landform on the plane of the field plot

(b) Without surface charge

(c) With surface charge for $\Gamma = 2\pi \times 10^7$ rad/s
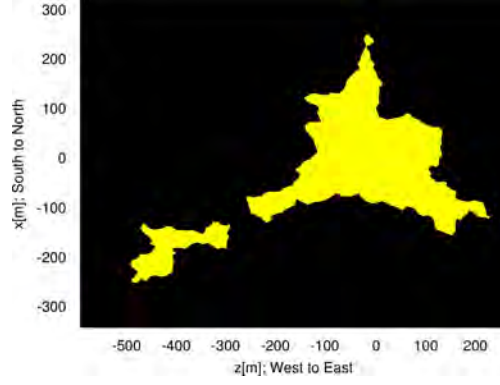

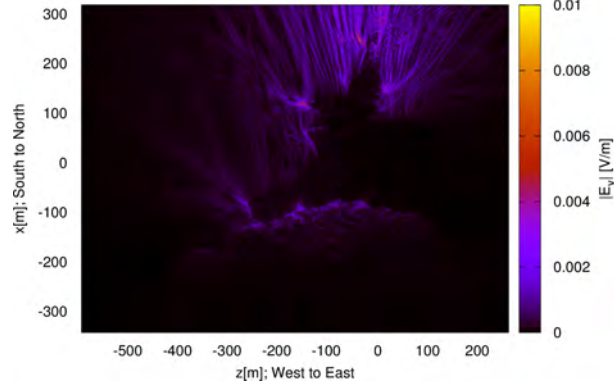(d) With surface charge for $\Gamma = 2\pi \times 10^8$ rad/s

Figure 7: FDTD analysis results of vertical component $|E_y|$ for the Oku-Hodakadake peak on the vertical plane from south to north including the peak. The incident wave is of horizontal E_z polarization.

the peak of the mountain. Therefore, the scattered or diffracted wave is stronger near the peak in Fig. 9 than that in Fig. 8. These results clearly show that the radio wave strongly interacts with the surface electrical charges. In addition, surface plasma waves are induced around the peak and they propagate towards the lower direction along the surface, being partly scattered by surface roughness, and diffracted repeatedly by the next lower peaks. Interestingly, the radio wave is scattered into various random directions in a beam-like form. This randomness in scattering and diffraction would cause randomness in detected signals at the observation point; sometimes detected but sometimes not, literally randomly, as the electrical charge density varies.

It should be noted that, in the case of $\Gamma = 2\pi \times 10^7$ in Figs. 7(c), 8(c) and 9(c), the analysis became unstable at a later time, and therefore terminated at an earlier time. This occurs exceptionally when the Drude dispersion has a small loss factor Γ and steep roughness exists in the landform in the long run of the analysis for a large-scale problem. These are difficult conditions for the numerical analysis to run stably by time marching. Such an instability problem did not occur for the other analyses in this section.
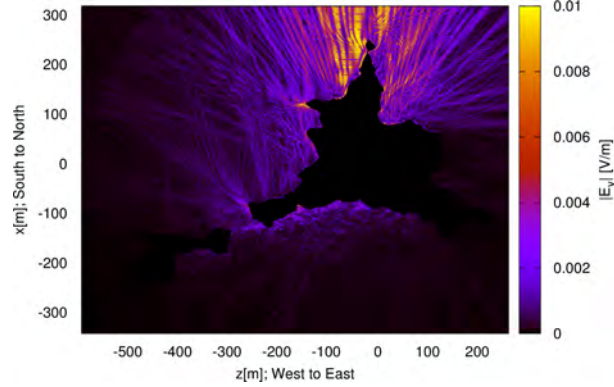
(a) Configuration of the landform on the plane of the field plot
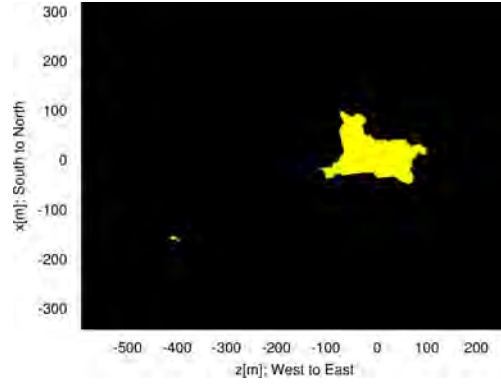

(b) Without surface charge
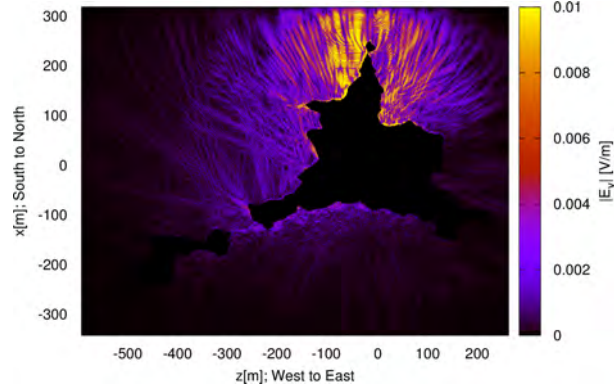
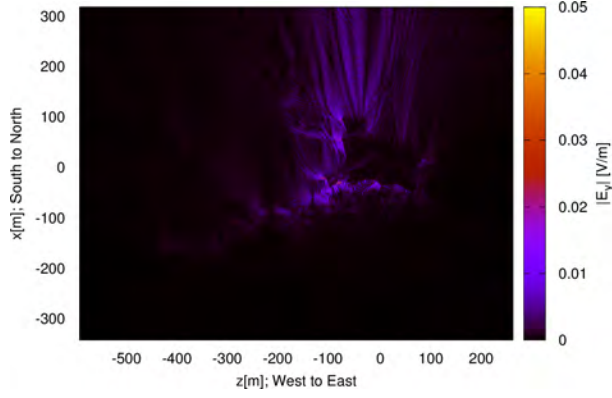(c) With surface charge for $\Gamma = 2\pi \times 10^7$ rad/s

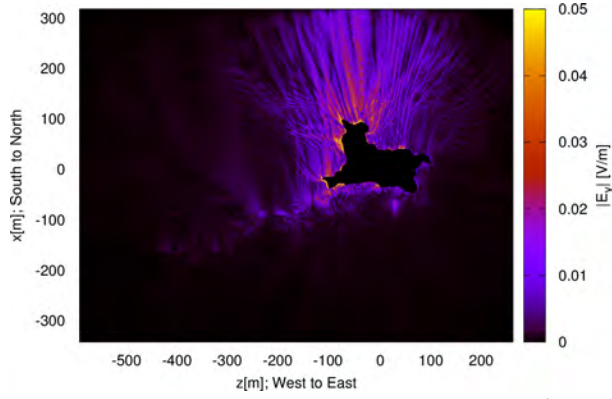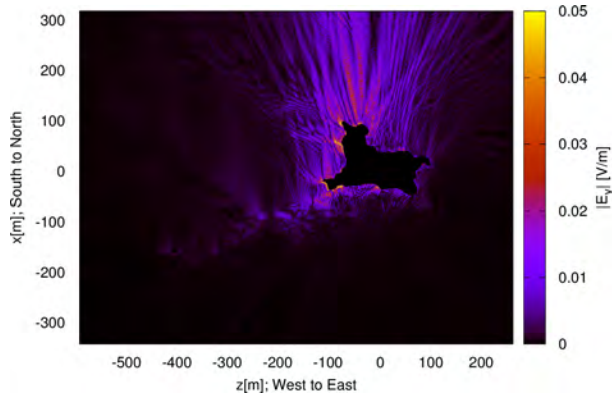(d) With surface charge for $\Gamma = 2\pi \times 10^8$ rad/s

Figure 8: FDTD analysis results of vertical component $|E_y|$ for the Oku-Hodakadake peak on the horizontal plane at an altitude of $3120\,\mathrm{m}$, which is $69.5\,\mathrm{m}$ down from the peak. The incident wave is of horizontal E_z polarization.

(a) Configuration of the landform on the plane of the field plot

(b) Without surface charge

(c) With surface charge for $\Gamma = 2\pi \times 10^7$ rad/s

(d) With surface charge for $\Gamma = 2\pi \times 10^8$ rad/s

Figure 9: FDTD analysis results of vertical component $|E_y|$ for the Oku-Hodakadake peak on the horizontal plane at an altitude of $3160\,\mathrm{m}$, which is $29.5\,\mathrm{m}$ down from the peak. The incident wave is of horizontal E_z polarization.

13

4 Precursors near Coastal Region along the Pacific Ocean in the Middle Part and Tonankai Area of Japan

In this section, we analyze the ground surface plasma wave in a coastal region, where the interaction with radio waves may differ apparently from that in the mountainous region in the previous section.

4.1 Observed Electromagnetic Precursors

As presented in the accompanying paper of Part I [4], we observed anomalous radio wave signals immediately before earthquakes occurred in Fukushima and Miyagi offshore, Japan, in 2021 and 2022. The signals were clearly and typically observed several hours to a few days before the earthquakes. We analyze the interaction between radio waves and ground surface plasma waves around a coastline instead of mountainous edges or peaks. The broadcast station, observation station, and analysis point are illustrated in Fig. 10. The analysis point was chosen approximately halfway between the broadcast station and the observation station because the point is on the Atsumi Peninsula and has a long cliff several tens of kilometers in length and several tens of meters in height along the Pacific Ocean. If the radio wave has a horizontal polarization, it is expected to interact via the vertical wall of the cliff between the radio wave and the ground surface plasma wave, thus strongly radiating horizontally polarized electromagnetic waves. The analysis point is also close to the Median Tectonic Line, which is the largest fault zone in Japan, running longitudinally from the west to the north-middle part of Japan. The radio wave from the Tsu broadcast station crosses over the Median Tectonic Line and reaches to the Iwata observation point.

The Tsu broadcast station (●, E136° 26'01", N34° 43'57", altitude 320m) is in Tsu City with a view toward the Atsumi Peninsula, where the analysis point (○) is located. The polarization of the broadcast wave is horizontal. The radio wave reaches the analysis point without a large obstacle. The Iwata observation station (■, E137° 49'20", N34° 39'20", altitude 4m) is located in Iwata City on the Pacific coastline. The Tsu broadcast station and the Iwata observation station are not on the direct line of sight, but by relaying at the middle point of the Atsumi Peninsula, it would be possible for the radio wave to reach the distance. Moreover, there will be no other obstacles disturbing the radio wave propagation once it is relayed.

4.2 Analysis of Coastal Region along the Pacific Ocean in the Middle Part of Japan

The analysis configuration of the middle part of the coastline of the Atsumi Peninsula is shown in Fig. 11. The size of the analysis region was $1420\,\mathrm{m}$ from west to east, $600\,\mathrm{m}$ from south to north, including a part of the Pacific Ocean. The height above sea level is $96\,\mathrm{m}$, added with tentative $2\,\mathrm{m}$-deep sea water and $2\,\mathrm{m}$-thick sea bottom, which will not affect the analysis results. Thus, the total height of the analysis region was $100\,\mathrm{m}$. The relative dielectric permittivity was set to $\epsilon_\infty = 6$ and the electric conductivity $\sigma = 1.0 \times 10^{-3}\,\mathrm{S/m}$ for the ground, and $\epsilon_\infty = 80$, $\sigma = 4.0\,\mathrm{S/m}$ for the sea water. The parameters of the Drude dispersion $f'_p = 408\,\mathrm{MHz}$ and two cases of $\Gamma = 2\pi \times 10^7\,\mathrm{rad/s}$ and $2\pi \times 10^8\,\mathrm{rad/s}$ were tested for the electrically-charged ground. The sea water was treated as a normal lossy conductive medium. The grid size of the DEM was approximately $5\,\mathrm{m}$, and it was refined by the spline interpolation to obtain the FDTD grid of $0.2\,\mathrm{m}$ resolution. The analysis region is surrounded by 50 layers of perfectly matched layer (PML) absorbing boundaries. The necessary total memory was $4.7\,\mathrm{TB}$ with 2304 CPU cores, and the elapsed time was approximately 16 hours for a single run of the analysis. No instability problems were observed for the analyses in this section.

Adjusting to the radio wave propagation path in Fig. 10, a radio wave of $70\,\mathrm{MHz}$ is incident from the west of the Atsumi Peninsula with a horizontal polarization of the E_x component. An
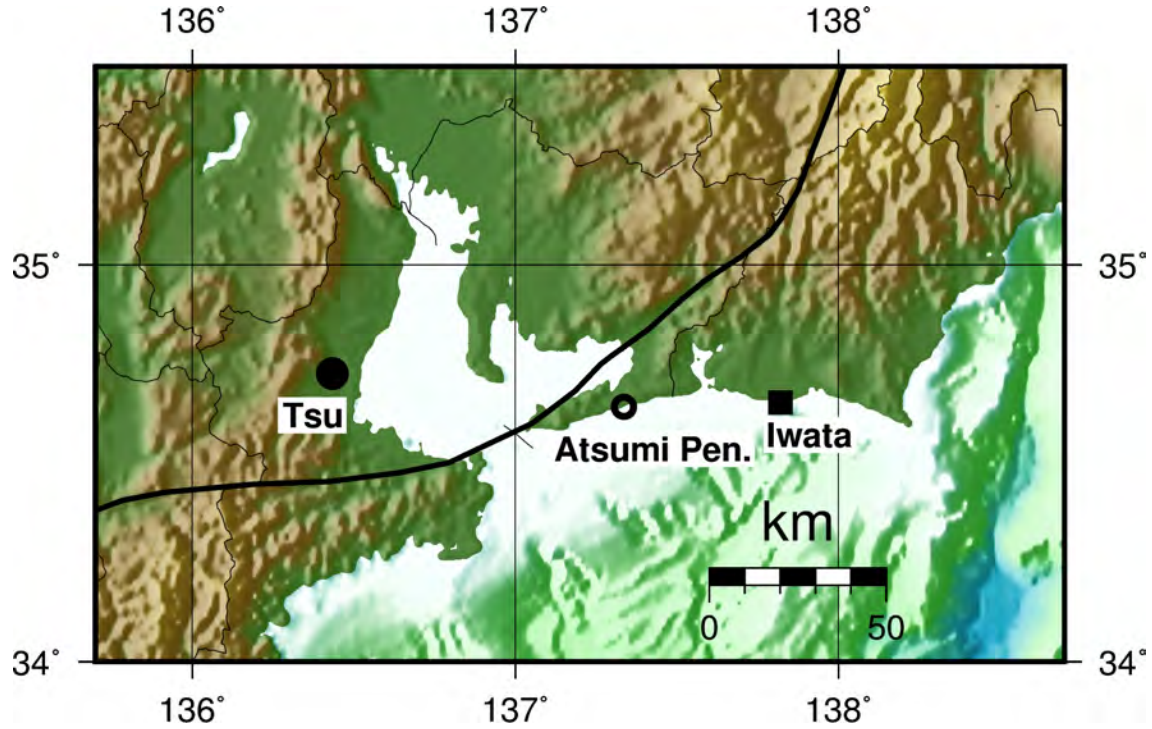
Figure 10: Map of the middle part of Japan around the broadcast station (●) in Tsu City, the observation station (■) in Iwata City, and the analysis point (○) in Toyohashi City in the Atsumi Peninsula facing the Pacific Ocean. Thick solid line is a part of the Median Tectonic Line. The map was generated with GMT and ETOPO1 dataset. Note the detail of the water surface in the map is partly inaccurate in the ETOPO1 dataset.
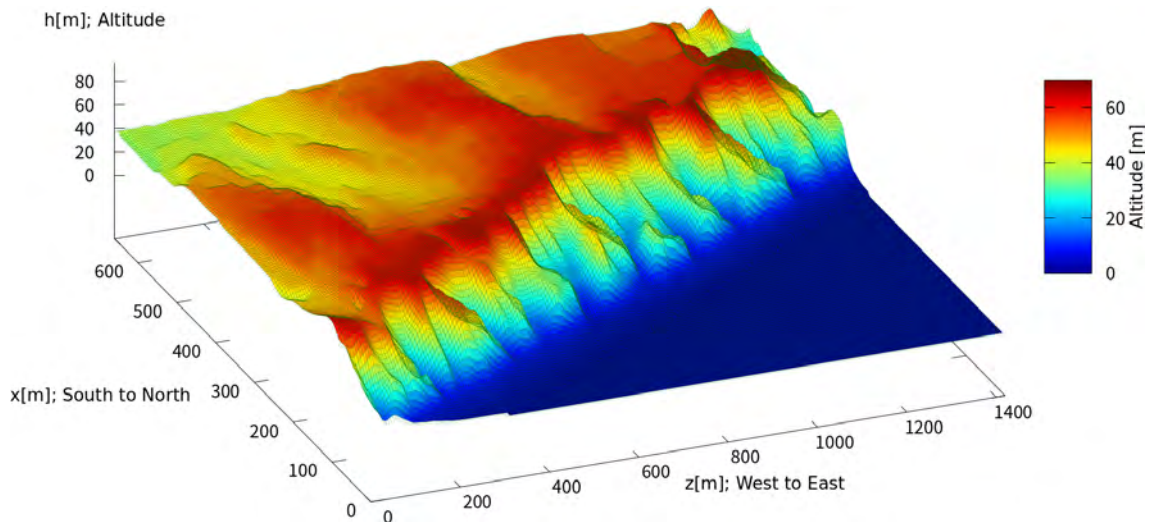

Figure 11: The 3D analysis configuration of a south coastline of the Atsumi Peninsula indicated in Fig. 10. Green grid lines show the original digital elevation model of approximately 5 m resolution publicized by the Geographical Survey Institute, Japan.

15

incident radio wave is given only at the south-half region of the analysis model, i.e., within the range of $x = 60\,\mathrm{m}$ to $360\,\mathrm{m}$, and only at the upper part of $y = 66\,\mathrm{m}$ to $91\,\mathrm{m}$, so that the radio wave comes horizontally from the west. In Figs. 12 and 13, the other horizontally polarized component of E_z is shown; by plotting the E_z component, the incident E_x component of large intensity does not disturb the appearance of the scattered and the diffracted waves, thus the comparison becomes easier between the cases with and without the surface charges. On the surface of the coastline of the Atsumi Peninsula in Fig. 12, it is found that the horizontally polarized field is scattered strongly if electric charges exist. In particular, Fig. 12(c) shows that radio waves are scattered in various directions owing to the complicated landform. If Γ is larger by an order of magnitude, Fig. 12(d) shows that the scattered and/or diffracted waves are still much stronger than those in the case of no surface charge, as shown in Fig. 12(b). In Fig. 13, a similar tendency is observed as shown in Fig. 12, even several meters above the ground.

The plot of the incident field component of E_x clearly shows in Fig. 14(c) that the strong scattered field appears at a point somewhat distant from the incident wave compared with the other cases of Fig. 14. Thus, in general, if strong scattering and diffraction exist along a coastline of tens of kilometers, the strength of the scattered and/or diffracted signal would become large enough to be detected. The analysis results in this section show a possible mechanism for the strong precursory signals in the horizontal polarization observed beyond the coastlines.
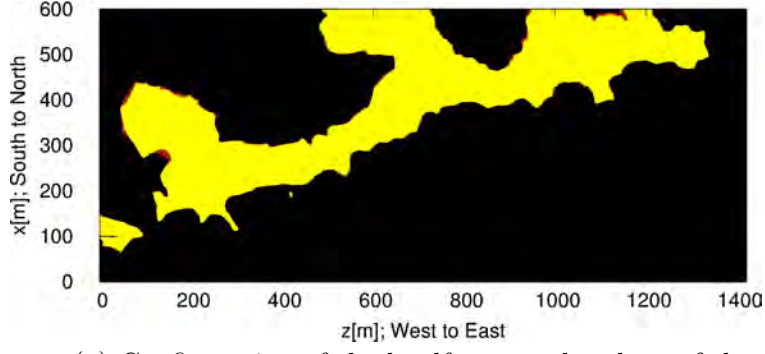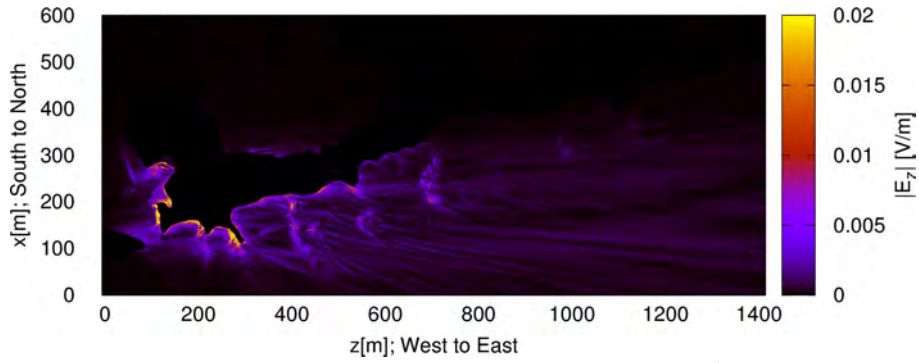
(a) Configuration of the landform on the plane of the field plot
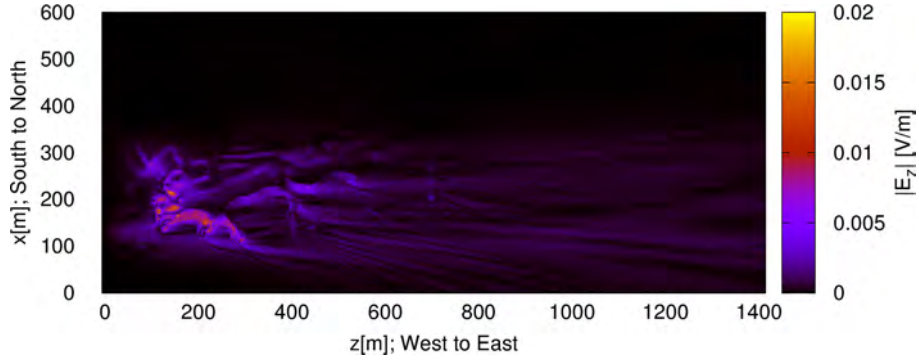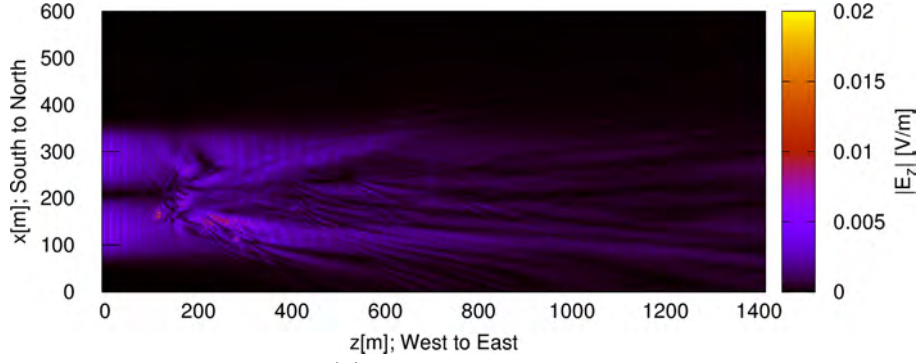

(b) Without surface charge
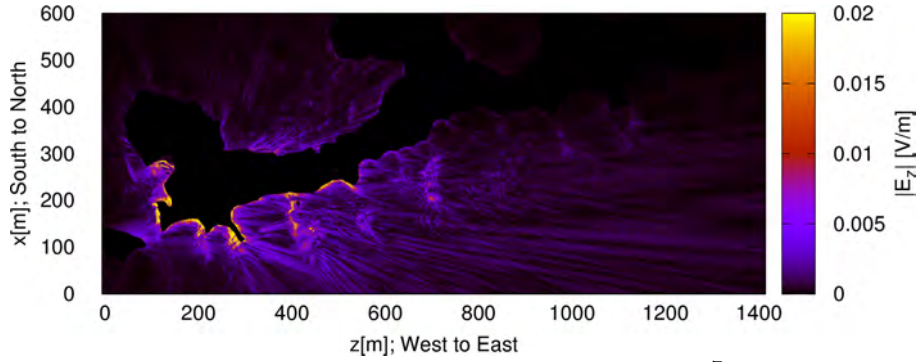
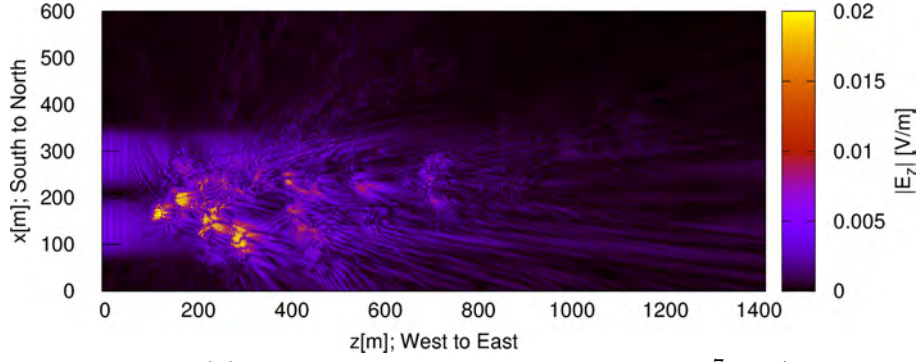(c) With surface charge for $\Gamma = 2\pi \times 10^7$ rad/s

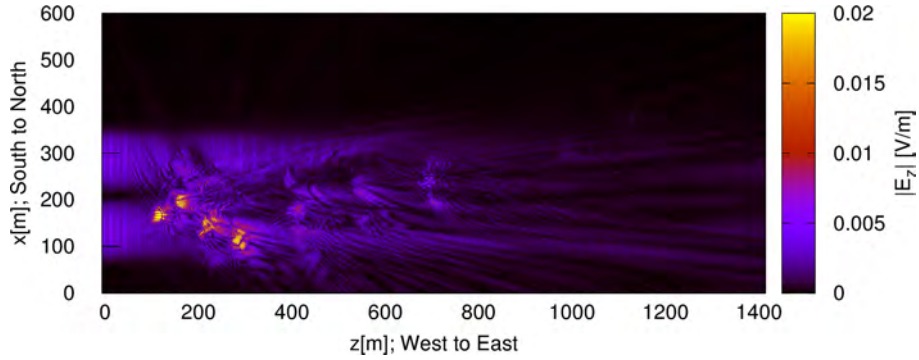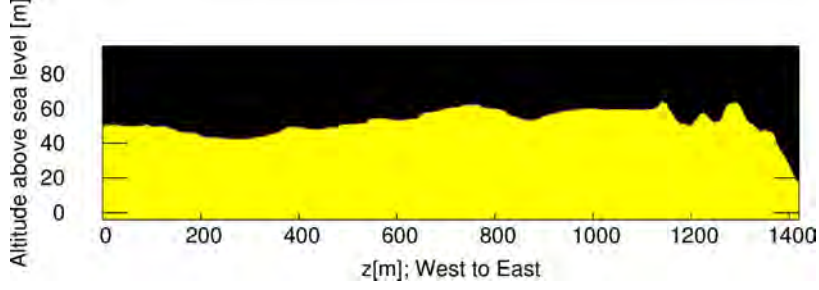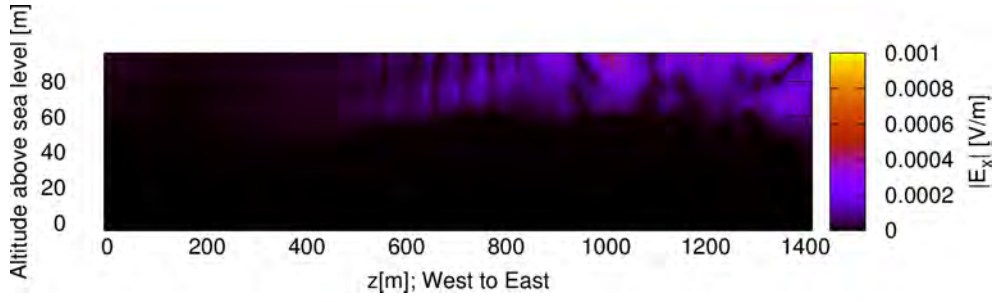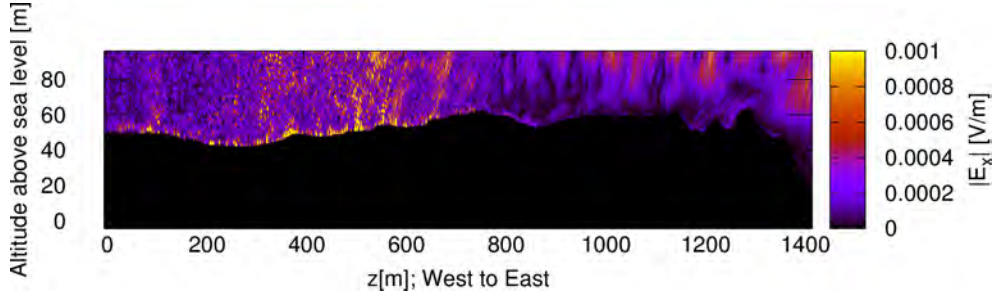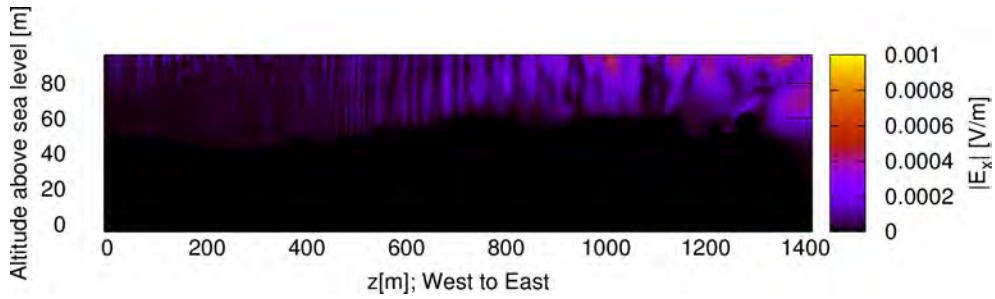(d) With surface charge for $\Gamma = 2\pi \times 10^8$ rad/s

Figure 12: FDTD analysis results of the coastline of the Atsumi Peninsula on the horizontal plane at an altitude of 56 m above sea level. The incident wave is of horizontal E_x polarization radiated from the west, and horizontal E_z component is plotted.

17

(a) Without surface charge

(b) With surface charge for $\Gamma = 2\pi \times 10^7$ rad/s

(c) With surface charge for $\Gamma = 2\pi \times 10^8$ rad/s

Figure 13: FDTD analysis results of the coastline of the Atsumi Peninsula on the horizontal plane at an altitude of $76\,\mathrm{m}$ above sea level. The incident wave is of horizontal E_x polarization radiated from the west, and horizontal E_z component is plotted. No cross section of the landform exists at this height.

(a) Configuration of the landform on the vertical plane at $x = 480\,\mathrm{m}$

(b) Without surface charge

(c) With surface charge for $\Gamma = 2\pi \times 10^7\,\mathrm{rad/s}$

(d) With surface charge for $\Gamma = 2\pi \times 10^8\,\mathrm{rad/s}$

Figure 14: FDTD analysis results of the coastline of the Atsumi Peninsula on the vertical plane at $x = 480\,\mathrm{m}$ in Fig.11. The incident wave is of horizontal E_x polarization radiated from the west, and the same horizontal E_x component is plotted at a location apart from the incident wave.

19

5 Precursors near Coastal Region on the Japan Sea Side in the Middle Part of Japan

We analyze another landform of the coast that is on the opposite side of Japan from the Pacific Ocean, which faces the west sea or Japan Sea in the middle part of Japan.

5.1 Observed Electromagnetic Precursors

In our associated paper of Part I [4], precursory signals were obtained in the radio wave signals on the propagation path analyzed in this section. A map of this region is shown in Fig. 15. The observation station ($\blacksquare$, E137° 11'13", N36° 41'38", alt. 30m) is located in Toyama City and set on the top of a building, and the broadcast station is in Niigata City ($\bullet$, E138° 48'30", N37° 42'24", alt. 600m) both on the west-sea side of Japan. The analysis point ($\bigcirc$) in Itoigawa City is famous for the north end of the Shizuoka-Itoigawa Tectonic Line. As in the previous section, the broadcast station and observation point in this section are slightly more distant than the line of sight; the landform halfway between them may scatter waves to yield a subtle change in the radio wave propagation between the cases with and without surface charges. It is also noted that the radio wave from the Niigata broadcast station crosses over the Shizuoka-Itoigawa Tectonic Line and reaches the Toyama observation point. The gigantic tectonic line may play a key role in conducting electrical charges from a distant earthquake hypocenter, which mechanism is not contradictory with the practically observed precursory signals.

5.2 Analysis of Coastal Region on the Japan Sea Side in the Middle Part of Japan

The analysis configuration of the landform is shown in Fig. 15. The size of the analysis region was 650 m from west to east, 300 m from south to north. The height above sea level is 190 m, and below sea level is tentatively set as 2 m-deep sea water and 2 m-thick sea bottom, thus, 194 m in total height. The material parameters are the same as the previous section, $\epsilon_\infty = 6$, $\sigma = 1.0 \times 10^{-3}$ S/m for the ground, and $\epsilon_\infty = 80$, $\sigma = 4.0$ S/m for the sea water. The parameters of the Drude dispersion $f_p' = 408$ MHz, and three cases of $\Gamma = 2\pi \times 10^6$ rad/s, $2\pi \times 10^7$ rad/m and $2\pi \times 10^8$ rad/s were tested for the electrically-charged ground. The sea water is always set as a normal non-Drude lossy conductive medium. The necessary computational resource was 3.4 TB memory with 2304 CPU cores, and the elapsed time was approximately 5 hours for a single run of the analysis.

The incident wave is chosen to be 70 MHz with the horizontally polarized E_x component radiated from east to west, from the rectangular source region from $x = 30$ m to 370 m, and from $y = 112.4$ m to 180.3 m, which simulates the actual radio wave path from the broadcast station in Niigata City. This analysis region has a large steep mountainous landform; thus, steep and rough slopes are close to the sea. The radio wave is usually blocked by the mountainous landform and would not directly reach the observation point. However, when electric charges exist, the radio wave propagates along the slopes, as seen in Fig. 17(d) and (e), which enables it to reach the observation point in Toyama City. It should be noted that the landform in this section has steep variations in its surface, which may not be visible to the eyes, but might have caused a numerical instability problem when the radio wave front reached a particular location in the analysis. This instability problem was independent of the values of Γ. The origin of the instability is a subject of our future research. The other field component E_z also shows the possibility of the radio wave propagation around the steep slopes to reach the observation point in Toyama City. The analysis results with surface charges for the three values of Γ plotted in Figs. 18(b) to (d) show more intense fields along the slope than the case without surface charges (a).
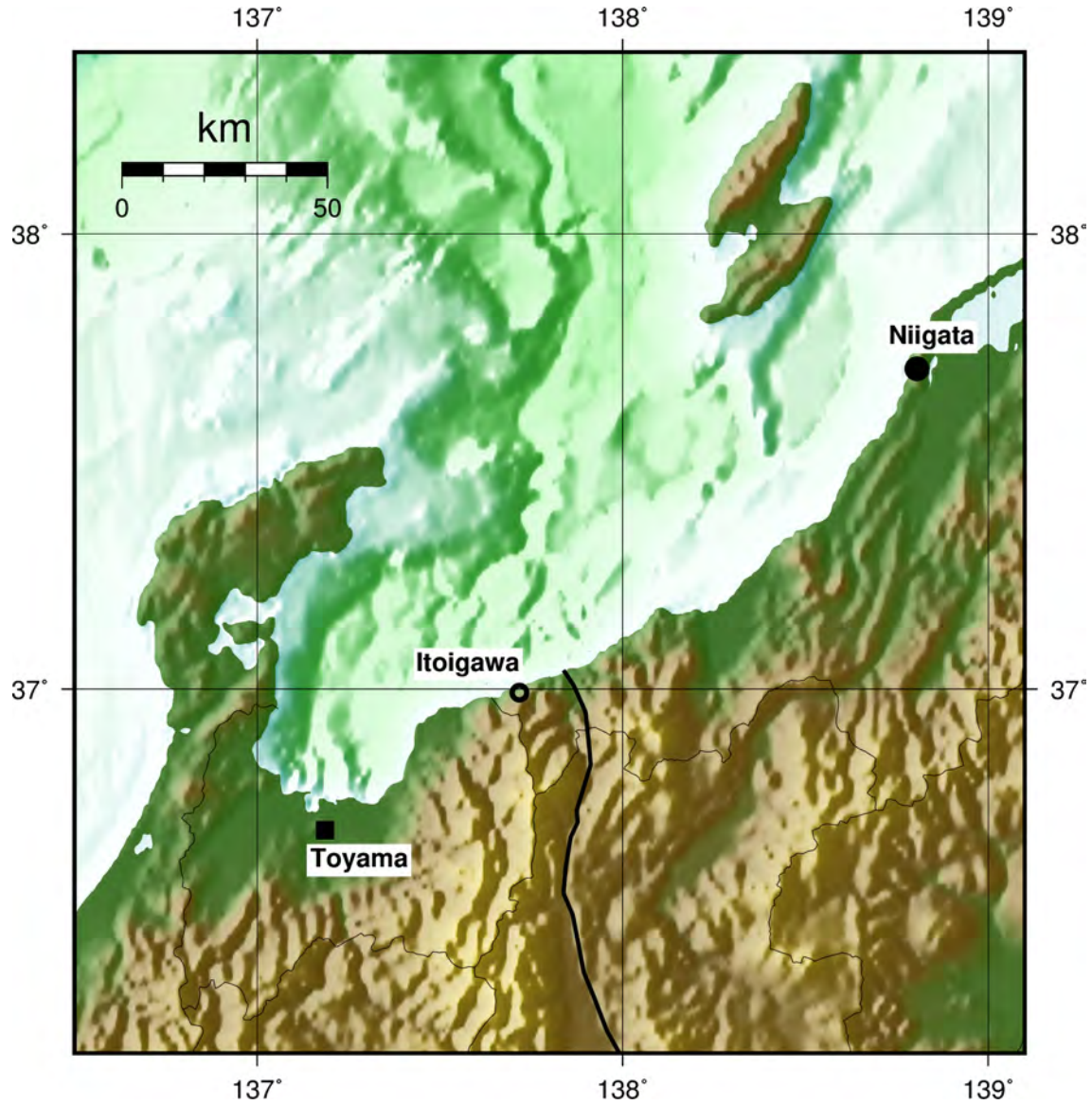
Figure 15: Map of the north-middle part of Japan around the broadcast station (●) in Niigata City, the observation point (■) in Toyama City, and the analysis point (○) in Itoigawa City along the west sea (Japan Sea) of Japan main island. Thick solid line is a part of the Shizuoka-Itoigawa Tectonic Line. The map was generated with GMT and ETOPO1 dataset. Note the detail of the water surface in the map is partly inaccurate in the ETOPO1 dataset.
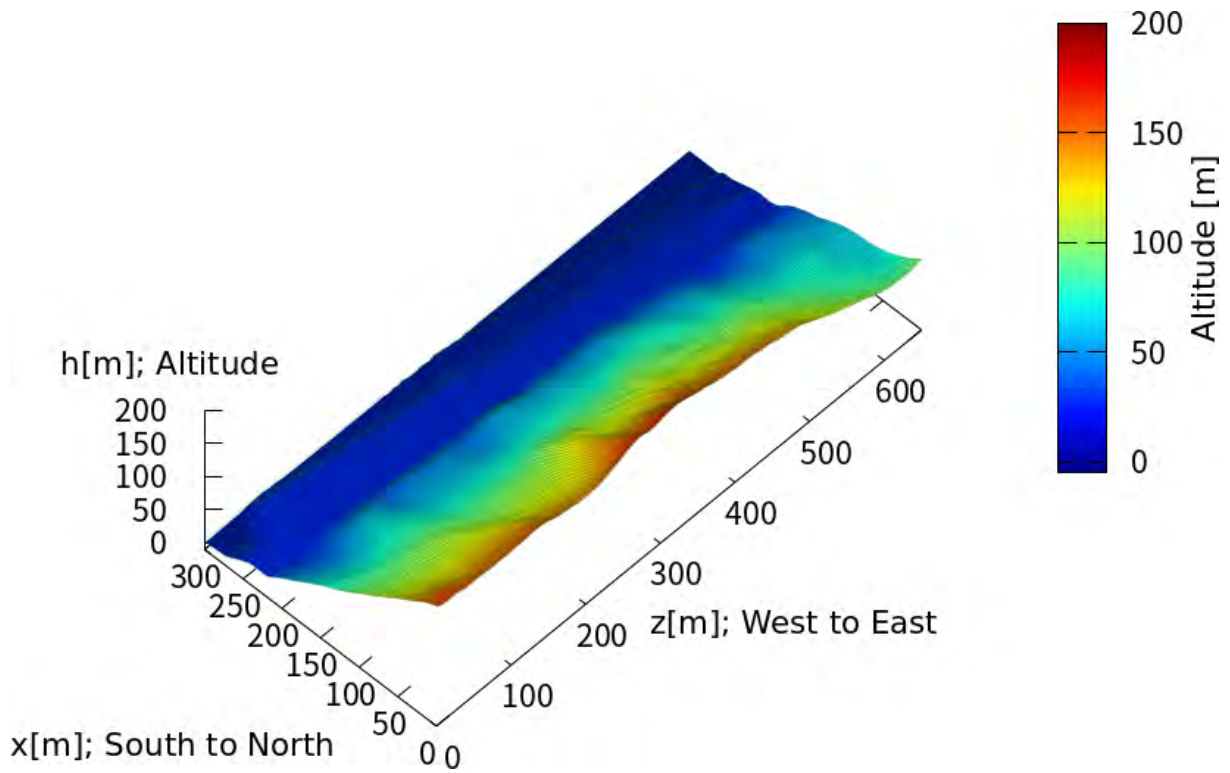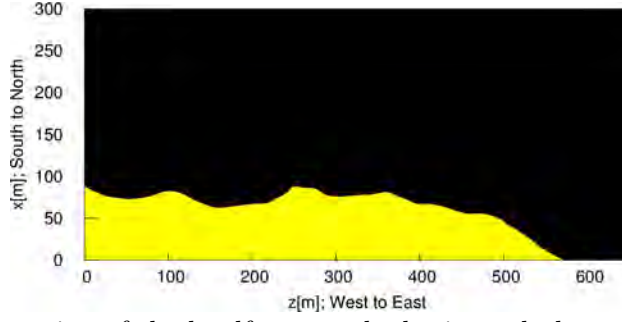
Figure 16: 3D analysis configuration of a coastline along the west sea (Japan Sea) side of Japan near Itoigawa City. Thin green grid lines show the re-sampled 2.5 m-resolution mesh for extracting the rectangular analysis region from the original digital elevation model of approximately 5 m resolution publicized by the Geographical Survey Institute, Japan.
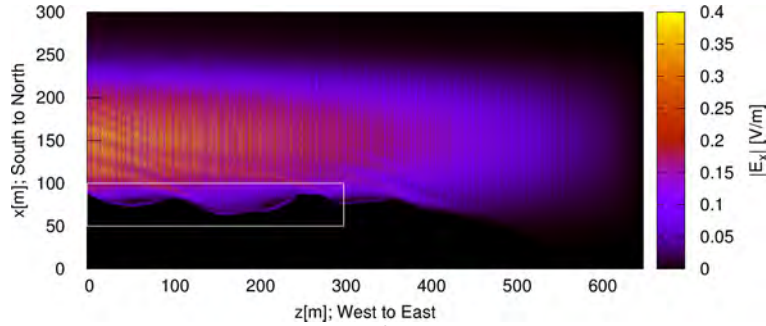
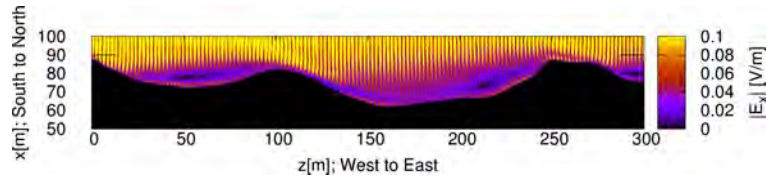(a) Configuration of the landform on the horizontal plane at an altitude of 112.4 m
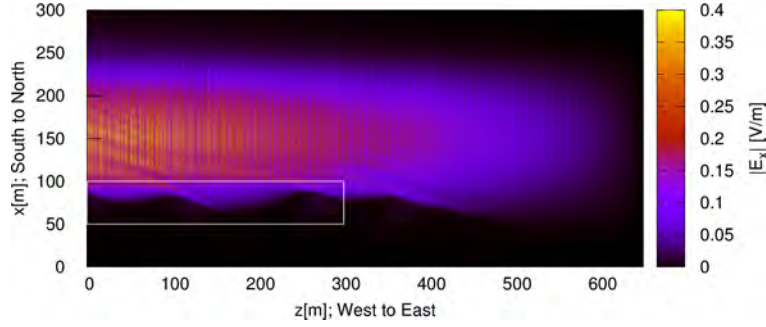
(b) Without surface charge, the white rectangular part of the wave propagation is to be contrasted.
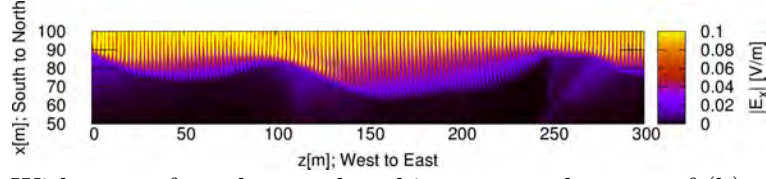
(c) Without surface charge, the white rectangular part of (b) expanded
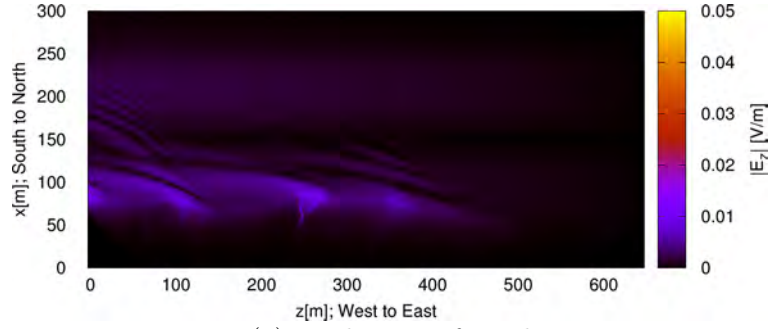

(d) With surface charge for $\Gamma = 2\pi \times 10^6$ rad/s, the white rectangular part of the wave propagation is to be contrasted.
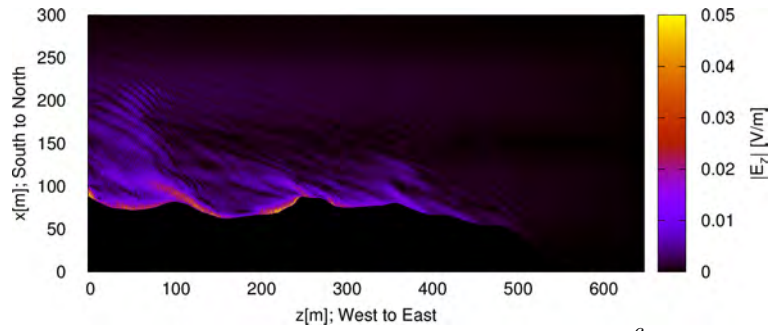

(e) With surface charge, the white rectangular part of (d) expanded

Figure 17: FDTD analysis results of the coastline along the west sea (Japan Sea) side of Japan on the horizontal plane at an altitude of 112.4 m above sea level. The incident wave is of horizontal E_x polarization radiated from the east, and the same horizontal E_x component is plotted.
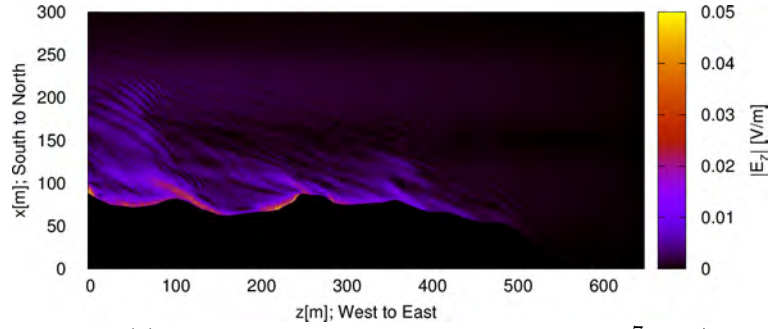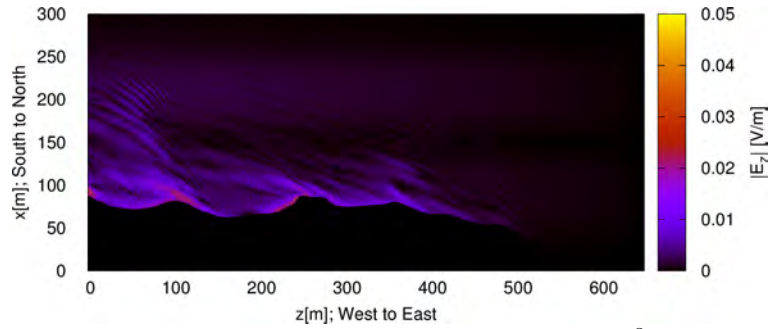
23

(a) Without surface charge

(b) With surface charge for $\Gamma = 2\pi \times 10^6$ rad/s

(c) With surface charge for $\Gamma = 2\pi \times 10^7$ rad/s

(d) With surface charge for $\Gamma = 2\pi \times 10^8$ rad/s

Figure 18: FDTD analysis results of the coastline along the west sea (Japan Sea) side of Japan on the same plane as in Fig.17. The incident wave is of horizontal E_x polarization radiated from the east, and the other horizontal E_z component is plotted.

6   Conclusions

We have analyzed the following three typical topographies of the ground, for which we have observed possible electromagnetic precursors of earthquakes: (i) a peak of a mountain close to an epicenter, (ii) a coastline with random cliffs near the Median Tectonic Line, and (iii) a coastline with steep mountainous slopes near the Shizuoka-Itoigawa Tectonic Line. All the landforms almost block the line-of-sight paths for the radio wave propagation. For all these cases, it is shown that electric charges on the ground interact strongly with the radio wave near the ground and that ground surface plasma waves are induced to cause anomalous scattering and diffraction of the radio wave. Thus, it is inferred that these are the mechanisms of the electromagnetic precursors of earthquakes that have been detected in our radio wave observations.

7   Open Research

Radio wave data and other environmental data integrated into synchronized diagrams by the authors are available at `http://www3.u-toyama.ac.jp/densou01/RadiowaveDataPlots_5.5c_nohighlight/RadiowaveDataPlots_Shizuoka_Iwata_all.pdf` and `http://www3.u-toyama.ac.jp/densou01/RadiowaveDataPlots_5.5c_nohighlight/RadiowaveDataPlots_Toyama_Toyama_all.pdf`.

Figures were made with Gnuplot version 5.2.8 available under Copyright by T. Williams, and C. Kelley at `http://www.gnuplot.info` [10].

The map was created using Generic Mapping Tools (GMT) version 5.4.5, under Copyright by The GMT Developers (2019 - 2022) available at `https://www.generic-mapping-tools.org` [9].

References

[1] M. Fujii. Theory of ground surface plasma wave associated with pre-earthquake electrical charges. *Radio Science*, 48:122–130, Mar. 2013.

[2] M. Fujii. Fundamental correction of Mie's scattering theory for the analysis of plasmonic resonance of a metal nanosphere. *Phys. Rev. A*, 89(3):033805, Mar. 2014.

[3] M. Fujii. A new mode of radio wave diffraction via the terrestrial surface plasmon on mountain range. *Radio Science*, 51:1396–1412, Aug. 2016.

[4] M. Fujii. Electromagnetic precursors of earthquakes mediated by ground surface plasma wave part I: Stable low-noise observation. 2022. submitted.

[5] M. Kamogawa and Y. Ohtsuki. Plasmon model for origin of earthquake related electromagnetic wave noises. *Proc. Japan Acad.*, 75(B):186–189, 1999.

[6] C. Kittel. *Introduction to solid state physics*. John Wiley and Sons, Inc., New York, 6th edition, 1986.

[7] J. Scoville, J. Sornette, and F. Freund. Paradox of peroxy defects and positive holes in rocks part II: Outflow of electric currents from stressed rocks. *J. of Asian Earth Sciences*, 114-2:338–351, Dec. 2015.

[8] S. Uyeda, T. Nagao, Y. Orihara, T. Yamaguchi, and I. Takahashi. Geoelectric potential changes: Possible precursors to earthquakes in japan. *PNAS*, 97(9):4561–4566, 2000.

[9] P. Wessel. The generic mapping tools.

[10] T. Williams and C. Kelley. Gnuplot homepage.